


Landau-Zener-Stückelberg interferometry in dissipative circuit quantum electrodynamicsMariano Bonifacio ¹, Daniel Domínguez,¹ and María José Sánchez^{1,2}¹*Centro Atómico Bariloche and Instituto Balseiro (Universidad Nacional de Cuyo), 8400 San Carlos de Bariloche, Río Negro, Argentina*²*Instituto de Nanociencia y Nanotecnología (INN), CONICET-CNEA, Argentina*

(Received 2 March 2020; revised manuscript received 29 May 2020; accepted 1 June 2020; published 15 June 2020)

We study Landau-Zener-Stückelberg (LZS) interferometry in a cQED architecture under the effects of dissipation. To be specific, we consider a superconducting qubit driven by a dc + ac signal and coupled to a transmission line resonator, but our results are valid for general qubit-resonators devices. To take the environment into account, we assume that the resonator is coupled to an Ohmic quantum bath. The Floquet-Born-Markov master equation is numerically solved to obtain the dynamics of the system for an arbitrary amplitude of the drive and different timescales. We unveil important differences in the resonant patterns between the strong coupling and ultrastrong coupling regimes in the qubit-resonator interaction, which are mainly due to the magnitude of photonic gaps in the energy spectrum of the system. We identify in the LZS patterns the contribution of the qubit gap and the photonic gaps, showing that for large driving amplitudes the patterns present a weaving structure due to the combined intercrossing of the different gaps contributions.

DOI: [10.1103/PhysRevB.101.245415](https://doi.org/10.1103/PhysRevB.101.245415)**I. INTRODUCTION**

Circuit quantum electrodynamics (cQED) [1–4]—the study of the interaction between superconducting circuits behaving as artificial atoms and transmission line resonators—has become one of the test beds for quantum information processing tasks [5]. Originally implemented for studying on-chip light-matter interactions, the enormous advances during the last decade in the development of long-lived qubits-resonators devices, have shown the possibility of performing a large number of high-fidelity quantum gates, entangling and coupling distant qubits to realize two qubit gates and to carry out nondemolition readout operations [6–16].

Landau-Zener-Stückelberg (LZS) interferometry has been established as a powerful tool to probe the energy level spectrum of a superconducting qubit and to study coherent phenomena for large driving amplitudes [17]. In typical LZS protocols, the qubit energy levels are modulated back and forth through an avoided crossing at a frequency faster than the qubit decoherence rate. Strong driving dynamic has been experimentally investigated in superconducting qubits [18–22], Cooper pair boxes and quantum dots devices [23–27]. In addition, LZS interferometry was recently proposed to determine relevant information related to the coupling of a qubit with a noisy environment [27–32].

In the present work, we analyze LZS conditions in cQED, by strongly driving a qubit coupled to a quantum mode of an oscillator. We take into account the coupling of the system to a quantum bath and study the dissipative dynamics in the strong qubit-resonator coupling using the Floquet-Markov master equation [31,33,34]. We focus in the strong driving regime (large driving amplitudes), beyond standard approaches that restrict the driven dynamics to the rotating wave approximation (RWA). In this way, we analyze the emergence of the multi-Floquet modes in the dissipative scenario of cQED, unveiling the interference patterns and population features

that are not captured within the RWA. In addition, our work complements previous ones focused on the analysis of dissipative Landau Zener transitions—for a constant velocity driving—in cQED [35]. Alternative driving schemes have been also implemented in cQED, like the periodic latching modulation of a transmon studied in Ref. [36]. Although we use parameters typical for superconducting qubits and microwave resonators experiments [37], our study can be extended to analyze Floquet spectroscopic experiments recently implemented in driven qubits coupled to mechanical resonators and for high or low-frequency driving fields [38].

The paper is organized as follows. In Sec. II, we introduce the driven cQED model Hamiltonian for the case of a flux qubit driven by an ac flux. We discuss the structure of the energy spectrum in the absence of driving, which will be useful to understand the emergence of multi-Floquet modes under the driving protocol. Section III is devoted to analyze the LZS interference patterns neglecting dissipation, with the aim of comparing the patterns that emerge due to the photonic gaps in the driven Jaynes Cummings model valid under the RWA, with those of the full driven Rabi Hamiltonian, where the counter rotating terms in the qubit-resonator interaction are taken into account. In Sec. IV, we extend the analysis to the dissipative case, which is relevant for realistic experimental situations. The strong coupling (SC) and ultrastrong coupling (USC) in the qubit-resonator interaction are analyzed in detail and the structure of the respective LZS patterns are characterized for finite times and in the stationary regime, after full relaxation with the bath degrees of freedom. A concluding summary is provided in Sec. V.

II. MODEL HAMILTONIAN

We consider a flux qubit driven by an ac harmonic flux and coupled capacitively to a transmission line resonator that contains one mode of the EM field, as customary

in cQED architectures [9,37,39]. The correspondent model Hamiltonian is

$$H(t) = H_q(t) + H_r + H_{qr}, \quad (1)$$

where

$$\begin{aligned} H_q(t) &= \frac{1}{2}[\varepsilon(t)\sigma_z + \Delta\sigma_x], \\ H_r &= \omega_r a^\dagger a, \\ H_{qr} &= g\sigma_y(a + a^\dagger), \end{aligned} \quad (2)$$

are the terms for the driven flux qubit restricted to a two-level system [31], the resonator and the Rabi interaction Hamiltonians, respectively. We take $\hbar = 1$ in this work. The qubit is driven by a time dependent bias $\varepsilon(t) = \varepsilon_0 + A \cos \omega t$, where ε_0 is the static bias component on top of which is the harmonic ac modulation of amplitude A and frequency ω [17,22,31,32]. The operators σ_x , σ_y , and σ_z are the Pauli matrices and Δ is the coupling strength between the states $|\uparrow\rangle$ and $|\downarrow\rangle$ of the computational basis of the qubit. In the absence of driving, the qubit Hamiltonian H_q has eigenenergies $\pm\omega_q/2$, with $\omega_q = \sqrt{\varepsilon_0^2 + \Delta^2}$. The frequency of the resonator is ω_r and a^\dagger (a) is the creation (annihilation) operator for resonator photons. The capacitive coupling between the flux qubit and the resonator here studied [37,39] is represented in terms of the σ_y operator, being g the coupling strength. Other well studied cases, like a charge qubit coupled capacitively to a resonator [1,2] or a flux qubit coupled inductively to a resonator [40] are modeled in terms of the operator σ_z in H_{qr} . For the composite Hilbert space $\mathcal{H}_{\text{qubit}} \otimes \mathcal{H}_{\text{resonator}}$ we use the product state basis $\{|\downarrow, n\rangle, |\uparrow, n\rangle\}_{n \in \mathbb{N}}$, where n is the eigenvalue of the resonator photon number operator $a^\dagger a$.

Throughout this work we will consider $\Delta/\omega_r = 0.0038$, which corresponds to typical experiments in driven flux qubits with small qubit gap [18], where $\Delta \sim 10\text{--}50$ MHz, while typical cavity frequencies are in the range of $\omega_r/2\pi \sim 10$ GHz [1]. In spite of these specific parameters, our results can be easily extended to other types of superconducting qubits. We study different values of the coupling parameter in the range $g/\omega_r = 0.0019\text{--}0.1125$. All relevant parameters are summarized in the following table.

Parameters of the Driven Rabi model.

Parameter	Value (in units of ω_r)
Δ	0.0038
ω	0.0375
g	0.0019–0.1125
ω_r	1

In cQED, it is customary to define the strong coupling (SC) and ultrastrong coupling (USC) regimes, with the conditions $g \lesssim 0.1\omega_{q/r}$ and $g > 0.1\omega_{q/r}$, respectively [5,41]. The USC regime has been experimentally achieved in recent years with superconducting qubits enabling the study of exciting and novel phenomena in the field of light-matter interaction [5,42,43].

Before focusing on the driven dynamics we analyze the structure of the energy spectrum in the absence of driving, i.e., by replacing $\varepsilon(t) \rightarrow \varepsilon = \varepsilon_0$ in the Hamiltonian of Eq. (1).

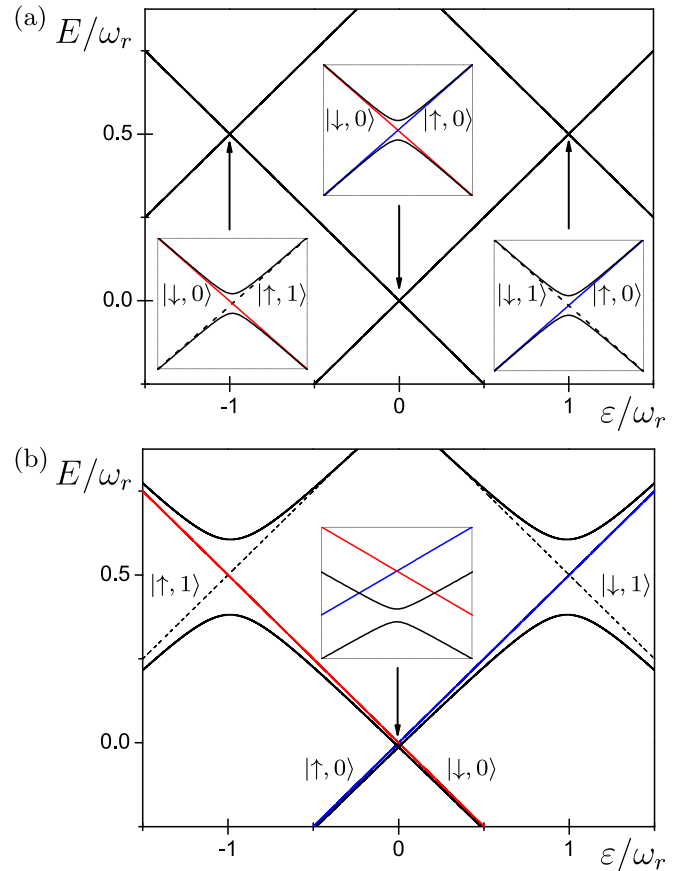


FIG. 1. Lowest energy levels of the Rabi Hamiltonian Eq. (1) without driving ($A = 0$), as a function of the dc bias $\varepsilon = \varepsilon_0$, for the parameters $\Delta/\omega_r = 0.0038$. (a) $g/\omega_r = 0.0019$ (SC) and (b) $g/\omega_r = 0.1125$ (USC) (solid lines). The qubit gap is at $\varepsilon = 0$ while the photonic gaps are at $\varepsilon = \pm\omega_r$. The color (dashed) lines are the energies $\pm\varepsilon/2$ ($\pm\varepsilon/2 + \omega_r$) of the product states $|\uparrow, 0\rangle$ and $|\downarrow, 0\rangle$ ($|\uparrow, 1\rangle$ and $|\downarrow, 1\rangle$) in the absence of qubit-resonator coupling ($g = 0$) and for $\Delta = 0$.

As we will show in the following sections this analysis will be useful to interpret the interference LZS patterns once the driving is included. In Fig. 1, we plot the three lowest energy levels as a function of ε , obtained after the numerical diagonalization of the Hamiltonian in the SC and the USC regimes, by choosing respectively $g/\omega_r = 0.0019$ (SC) and 0.1125 (USC). The qubit-resonator interaction mixes the states of the product basis in a nontrivial way. However, away from the avoided crossings and for the parameters considered in this work, the eigenenergies can be approximated by $\pm\varepsilon/2 + n\omega_r$. The associated eigenstates, spanned in the product basis, have weight mainly on the states $|\uparrow, n\rangle$ and $|\downarrow, n\rangle$, respectively, with n the number of photons in the resonator.

Due to the $\frac{\Delta}{2}\sigma_x$ term in the Hamiltonian H_q of Eq. (2), “qubit gaps” of magnitude Δ open at $\varepsilon = 0$. Additionally, “photonic gaps” $\Delta_n \approx 2g\sqrt{n+1}$ open at $\varepsilon = \pm\omega_r$ as a result of the qubit-resonator interaction [1].

Our analysis goes beyond the dispersive regime, $g \ll |\varepsilon - \omega_r| \ll |\varepsilon + \omega_r|$, which is usually employed for nondemolition readout of the qubits in typical cQED proposals [1]. In that scheme, the resonator experiences a frequency shift that

depends on the qubit state. Thus the state of the qubit can be read out indirectly by performing measurements on the resonator [5]. However, this technique relies on the use of an effective Hamiltonian and the range of parameters where the approximation is valid is restricted, while we report general results for arbitrary parameters.

III. LZS INTERFEROMETRY

In order to study the LZS interferometry in cQED, we now include the time dependent bias $\varepsilon(t) = \varepsilon_0 + A \cos \omega t$. To calculate the quantum dynamics of the full driven Rabi Hamiltonian, Eq.(1), we use the Floquet formalism [44] that allows for an exact treatment of time-periodic Hamiltonian $H(t) = H(t + \tau)$, with $\tau = 2\pi/\omega$ the period of the drive. In this formalism, the solutions of the Schrödinger equation $i \frac{d}{dt} |\psi(t)\rangle = H(t) |\psi(t)\rangle$ are expressed as $|\psi_\alpha(t)\rangle = e^{-i\varepsilon_\alpha t} |\alpha(t)\rangle$, where the Floquet states $|\alpha(t)\rangle$ and corresponding quasienergies ε_α are obtained from the eigenvalue equation $\mathcal{H} |\alpha(t)\rangle = \varepsilon_\alpha |\alpha(t)\rangle$, being $\mathcal{H} = H(t) - i\partial_t$ the Floquet Hamiltonian. The resulting Floquet states satisfy $|\alpha(t)\rangle = |\alpha(t + \tau)\rangle$ [45,46]. We obtain numerically the Floquet states and quasienergies following the same procedure as in Ref. [31].

In LZS interferometry, when a quantum system is driven through an energy-level avoided crossing of magnitude $\tilde{\Delta}$ by a periodic signal of amplitude A and frequency ω , the resonance condition, for which the transfer of population is maximum, depends on the velocity of passing through the avoided level crossing [17]. Usually, the slow driving regime is defined for $A\omega < \tilde{\Delta}^2$, while the fast driving condition is attained for $A\omega \gg \tilde{\Delta}^2$. In recent years, the specific features of the associated LZS resonance patterns have been studied and probed in driven qubits as both regimes have also been experimentally attained [27,47–50].

A. The driven Jaynes-Cummings Hamiltonian: photonic-LZS

In this section, we analyze the Hamiltonian defined by Eq. (2) under the assumption of $\Delta \ll \varepsilon_0 \sim \omega_r$ and for relative small driving amplitudes $A < \varepsilon_0$. These two conditions can be written in compact form as $\Delta \ll |\varepsilon_0| - A$, under which the term $\frac{A}{2} \sigma_x$ can be neglected in Eq. (2), as the system is always driven away from the qubit avoided crossing at $\varepsilon_0 = 0$. In this case, the separation of the energy levels of the qubit $\omega_q = \sqrt{\varepsilon_0^2 + \Delta^2}$ can be thus approximated by ε_0 .

In addition, assuming $\{g, |\omega_q - \omega_r|\} \ll |\omega_q + \omega_r|$, the qubit-resonator interaction $g\sigma_y(a^\dagger + a)$ can be replaced by $ig(\sigma_- a^\dagger - \sigma_+ a)$, as a result of a rotating wave approximation (RWA) [1,51,52], where σ_+ and σ_- are the raising and lowering operators for the qubit, respectively. This interaction conserves the number of excitations of the system qubit-resonator and makes possible to solve separately the dynamics for each of the two-dimensional subspaces spanned by $\{|\uparrow, n\rangle, |\downarrow, n+1\rangle\}_{n \in \mathbb{N}}$ and the single state $\{|\downarrow, 0\rangle\}$. Under these assumptions the driven Jaynes-Cummings (DJC) Hamiltonian, defined in each of the mentioned subspaces [1],

$$H_{JC}^{(n)}(t) = \left(n + \frac{1}{2}\right)\omega_r \begin{pmatrix} 1 & 0 \\ 0 & 1 \end{pmatrix} + \frac{1}{2} \begin{pmatrix} \delta(t) & -i\Delta_n \\ i\Delta_n & -\delta(t) \end{pmatrix}, \quad (3)$$

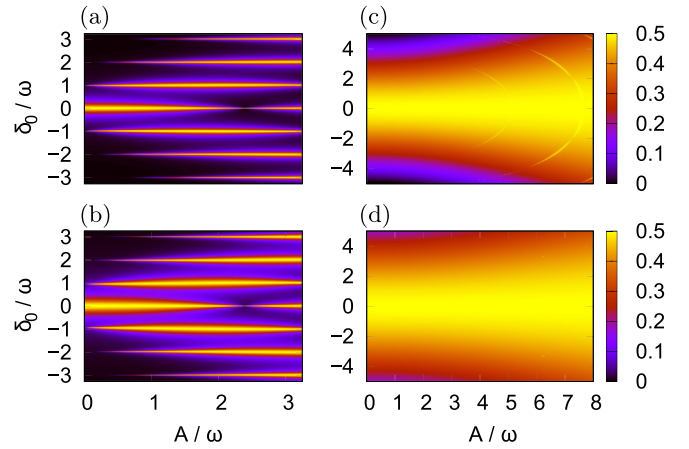


FIG. 2. Numerically obtained LZS interference patterns for the DJC Hamiltonian, Eq. (3). Plots of $\bar{P}_{|\downarrow, n+1\rangle \rightarrow |\uparrow, n\rangle}$ as a function of the driving amplitude A and dc bias δ_0 in units of ω , for $g/\omega_r = 0.0019$ and $n = 3$ (a) [$n = 10$ (b)] and $g/\omega_r = 0.1125$ and $n = 0$ (c) [$n = 1$ (d)].

is used to solve the system dynamics instead of the original driven Rabi Hamiltonian, Eq. (2). As a consequence the system can be studied as a collection of (noninteracting) driven two level systems with a photon-number dependent gap $\Delta_n = 2g\sqrt{n+1}$, and energies globally shifted. In Eq. (3), we have defined $\delta(t) \equiv \varepsilon(t) - \omega_r = \delta_0 + A \cos \omega t$, with $\delta_0 = \varepsilon_0 - \omega_r$.

In the following, we assume that the system is prepared at the initial time $t = 0$ in the product state $|\downarrow, n+1\rangle$. After calculating the Floquet states and quasienergies of $H_{JC}^{(n)}(t)$, we compute the time-averaged probability (averaged over a period of the driving) of finding the system in the $|\uparrow, n\rangle$ state, $\bar{P}_{|\downarrow, n+1\rangle \rightarrow |\uparrow, n\rangle} = \frac{1}{\tau} \int_0^\tau dt P_{|\downarrow, n+1\rangle \rightarrow |\uparrow, n\rangle}(t)$.

In Fig. 2, we show the numerical results for the intensity plot of $\bar{P}_{|\downarrow, n+1\rangle \rightarrow |\uparrow, n\rangle}$ as a function of the driving amplitude A and dc detuning δ_0 , for the SC and USC regime and for two different values of n . For $g/\omega_r = 0.0019$ [see Figs. 2(a) and 2(b)], as the photonic gap is small up to values of $n \gg 1$ ($\Delta_n \sim 0.01\sqrt{(n+1)\omega}$), the system is in the fast driving regime. In this case, the resonance condition is satisfied for $\sqrt{\delta_0^2 + \Delta_n^2} = m\omega$, which is the straightforward generalization of the usual resonance condition obtained for flux qubits in the fast driving regime [18,31,53]. For large detuning $\delta_0 \gg \Delta_n$, the m -resonance condition becomes $\delta_0 \approx m\omega$. Notice that the width of the resonance lobes in Figs. 2(a) and 2(b) depends on the photon number n , as the magnitude of the avoided crossing is $\Delta_n = 2g\sqrt{n+1}$. These LZS patterns can be qualitatively described by an analytical expression for the average probability near the m -resonance, $\bar{P}_{|\downarrow, n+1\rangle \rightarrow |\uparrow, n\rangle}^{\text{RWA}}$, originally derived for driven flux qubits in the fast driving and within a rotating wave approximation [17–19,32,54], and here trivially extended to analyze the DJC:

$$\bar{P}_{|\downarrow, n+1\rangle \rightarrow |\uparrow, n\rangle}^{\text{RWA}} = \frac{1}{2} \frac{[\Delta_n J_{-m}(\frac{A}{\omega})]^2}{[\delta_0 - m\omega]^2 + [\Delta_n J_{-m}(\frac{A}{\omega})]^2}. \quad (4)$$

This equation shows Lorentzian-shaped resonances with a maximum probability value of $\frac{1}{2}$ at $\delta_0 = m\omega$ and width $|\Delta_n J_{-m}(\frac{A}{\omega})|$, being $J_m(x)$ the m^{th} order Bessel function

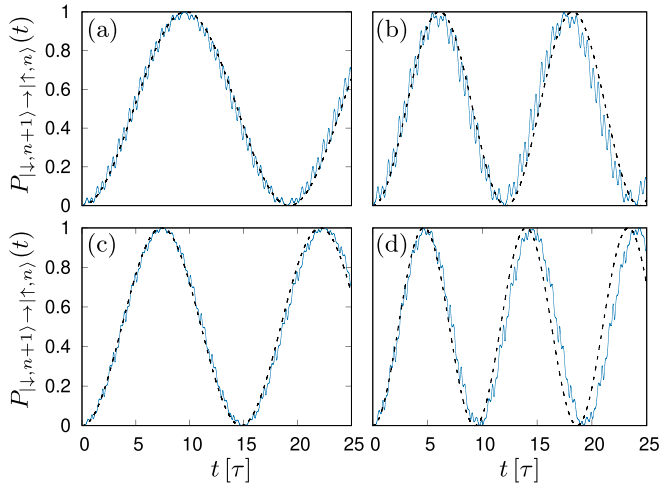


FIG. 3. Instantaneous transition probability $P_{|\downarrow, n+1\rangle \rightarrow |\uparrow, n\rangle}(t)$ for driving amplitude $A/\omega = 3$ and coupling $g/\omega_r = 0.0019$. (Top) Photon number $n = 3$ (a) and 10 (b) for resonance $\delta_0/\omega = 0$. (Bottom) Photon number $n = 3$ (c) and $n = 10$ (d) for resonance $\delta_0/\omega = 1$. The fast oscillations exhibited in the numerical results (solid line), are not captured by the RWA approximation, Eq. (5) (dashed line).

of the first kind. In particular, at the zeros of $J_{-m}(x)$ is $\bar{P}_{|\downarrow, n+1\rangle \rightarrow |\uparrow, n\rangle}^{\text{RWA}} = 0$, a phenomenon known as *coherent destruction of tunneling* [33].

Despite of the fact that the shape and positions of the resonances in Figs. 2(a) and 2(b) are captured by Eq. (4), the instantaneous transition probability $P_{|\downarrow, n+1\rangle \rightarrow |\uparrow, n\rangle}(t)$ depicted in Fig. 3 exhibits fast oscillations which are not reproduced by the RWA expression. Following Ref. [17], the instantaneous transition probability (near a m-resonance) between $|\downarrow, n+1\rangle$ and $|\uparrow, n\rangle$ can be written in the RWA as

$$P_{|\downarrow, n+1\rangle \rightarrow |\uparrow, n\rangle}^m(t) = \frac{1}{2} \frac{[\Delta_n J_{-m}(\frac{A}{\omega})]^2}{\Omega_m^2} (1 - \cos \Omega_m t), \quad (5)$$

being $\Omega_m = \sqrt{[\delta_0 - m\omega]^2 + [\Delta_n J_{-m}(\frac{A}{\omega})]^2}$ the generalized Rabi frequency. Equation (5) essentially captures the sinusoidal oscillations of Fig. 3, however, it fails in describing the fast oscillations which are associated to the Landau Zener transitions at the avoided crossing [54]. Notice that the period of these fast oscillations depends on the value n , which changes the effective gap Δ_n and therefore the instantaneous transition probability.

Upon increasing g or increasing n the photonic gap becomes much larger than the driving frequency ω and the LZS interferometry patterns correspond to the slow driving regime. In Figs. 2(c) and 2(d), we show the USC case for $g/\omega_r = 0.1125$, where already for $n = 0$ is $\Delta_n > \omega$. In this case, the resonances describe arcs around the point $A = 0$, $\delta_0 = 0$ and the resonance condition depends on the value A , in contrast to the fast driving regime [17,23,48,54]. Notice that for $n = 1$, the complete adiabatic regime (i.e., null transition probability to the excited state) is attained for the range of A and δ_0 values considered, and thus the average probability remains $\bar{P}_{|\downarrow, n+1\rangle \rightarrow |\uparrow, n\rangle} \sim 0.5$.

B. The driven Rabi Hamiltonian: combined photonic-LZS + qubit-LZS

Away from the regime analyzed in the previous section, the full driven Rabi (DR) Hamiltonian (2) has to be solved. The effect of the counter rotating terms become important either because of ultrastrong coupling or because of extremely large detuning, $\{g, |\omega_q - \omega_r|\} \sim |\omega_q + \omega_r|$. Under these conditions, the RWA that gave place to the DJC Hamiltonian, Eq. (3), breaks down [41,43,51].

In the following, we analyze the LZS interferometry patterns that emerge for the DR Hamiltonian, i.e., when the time dependence $\varepsilon(t) = \varepsilon_0 + A \cos \omega t$ is taken into account. As we will show, the different avoided crossings present in the spectrum of Fig. 1 will produce a richer and more complex structure in the LZS patterns in comparison to those obtained for the DJC effective two-level system.

In order to make the calculations numerically affordable, and without loss of generality in our analysis, we consider up to $n = 3$ photons and calculate the time-averaged probability, $\bar{P}_{|\uparrow\rangle}$, of measuring the qubit in the state $|\uparrow\rangle$ regardless the number of photons in the resonator, for the initial condition $|\downarrow, 0\rangle$, as a function of the driving amplitude A and the dc bias ε_0 .

Different resonance conditions—dependent on the driving amplitude A , the magnitude of the different gaps and their relative position with respect to the dc bias ε_0 —contribute to the interference patterns. A gap can mediate a LZS transition only if it is reached by the driving range ($\varepsilon_0 - A, \varepsilon_0 + A$). Therefore, for a given value of ε_0 and for increasing amplitudes starting at $A = 0$, different avoided crossings can be accessed [18,20].

We start by analyzing the intensity plot of $\bar{P}_{|\uparrow\rangle}$ for the SC regime ($g/\omega_r = 0.0019$), in terms of A and ε_0 . Figure 4(a) exhibits resonances characteristic of the fast driving [17,46].

Given a gap in the energy spectrum of magnitude $\tilde{\Delta}$ located at $\tilde{\varepsilon}$ and under fast driving regime, the m-resonance condition can be written as $\varepsilon_0 - \tilde{\varepsilon} \approx m\omega$, which is a generalization of the resonance condition for an isolated gap at $\tilde{\varepsilon} = 0$ [54]. Thus, in principle, one can use a generalization of Eq. (4) by replacing $\delta_0 \rightarrow \varepsilon_0 - \tilde{\varepsilon}$ in order to describe the resonance patterns associated to an isolated gap.

To understand the structure of Fig. 4(a), it is instructive to focus on the three lowest energy levels of the spectrum shown in Fig. 1(a). The qubit central gap separating the first and second levels is involved in the $|\downarrow, 0\rangle \leftrightarrow |\uparrow, 0\rangle$ transitions, with the associated qubit resonance condition $\varepsilon_0 = m\omega$. The photonic gap at $\varepsilon_0 = -\omega_r$ mediates $|\downarrow, 0\rangle \leftrightarrow |\uparrow, 1\rangle$ transitions, with a resonance condition given by $\varepsilon_0 = -\omega_r + m\omega$. On the other hand, the photonic gap at $\varepsilon_0 = \omega_r$ favors $|\uparrow, 0\rangle \leftrightarrow |\downarrow, 1\rangle$ transitions, with a resonance condition $\varepsilon_0 = \omega_r + m\omega$. The LZS interference associated with this later gap does not contribute to $\bar{P}_{|\uparrow\rangle}$ since in the present case we start with the initial condition $|\downarrow, 0\rangle$. The different qubit and photonic resonance conditions are thus organized along (shifted) horizontal lines, giving place to the pattern exhibited in Fig. 4(a), where the “qubit-LZS” interference pattern and the “photonic-LZS” interference pattern are combined.

In Fig. 5, we show a scheme depicting the boundaries of the regions where resonances associated to the qubit and photonic avoided crossings occur in $\bar{P}_{|\uparrow\rangle}$, as a function of the dc bias

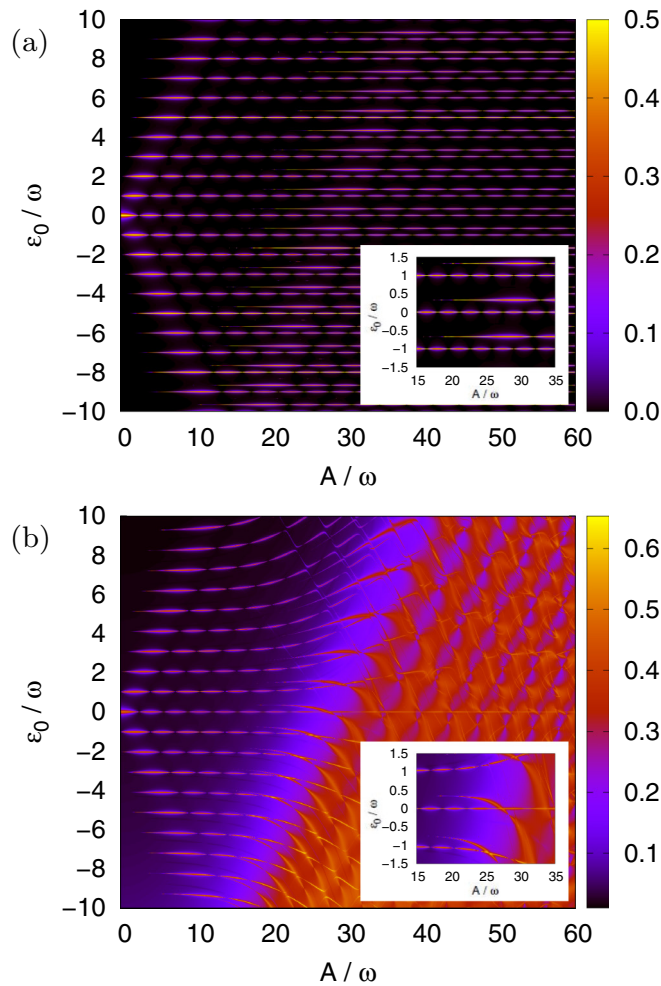


FIG. 4. Intensity plots of the LZS interference patterns for the driven Rabi Hamiltonian (2). Plots of $\bar{P}_{|\uparrow\rangle}$ as a function of the driving amplitude A and ϵ_0 , for (a) $g/\omega_r = 0.0019$ and (b) 0.1125 . The calculations were performed for $\omega/\omega_r = 0.0375$ and $\Delta/\omega_r = 0.0038$. The insets in both panels show the resonances patterns in more detail.

ϵ_0 and amplitude A . The dashed-line rectangle delimits the region of parameters considered in this work. We label six different regions according to the resonances that appear in the patterns. Following the description of Fig. 4(a), we see that regions I and II present no resonances. In region III, there is a pure qubit-LZS pattern with only the resonances mediated by the qubit gap at $\epsilon_0 = 0$. In region IV, coexist the combined qubit-LZS pattern and the photonic-LZS pattern associated to the gap at $\epsilon_0 = -\omega_r$. Analogously, in region V coexist the qubit-LZS pattern and the photonic-LZS pattern due to the gap at $\epsilon_0 = \omega_r$ (seen when the initial condition has components in $|\uparrow, 0\rangle$). Finally, region VI contains the combined qubit-LZS pattern and both photonic-LZS patterns.

Figure 4(b) exhibits the case of ultra strong coupling with $g/\omega_r = 0.1125$. We observe a different structure of resonances, as a consequence of the enlargement of the photonic gaps located at $\epsilon_0 = \pm\omega_r$. The resonances associated to the gap at $\epsilon_0 = -\omega_r$ form arcs around the point $A = 0$, $\epsilon_0 = -\omega_r = -26.667\omega$ [partially observed in the inset of

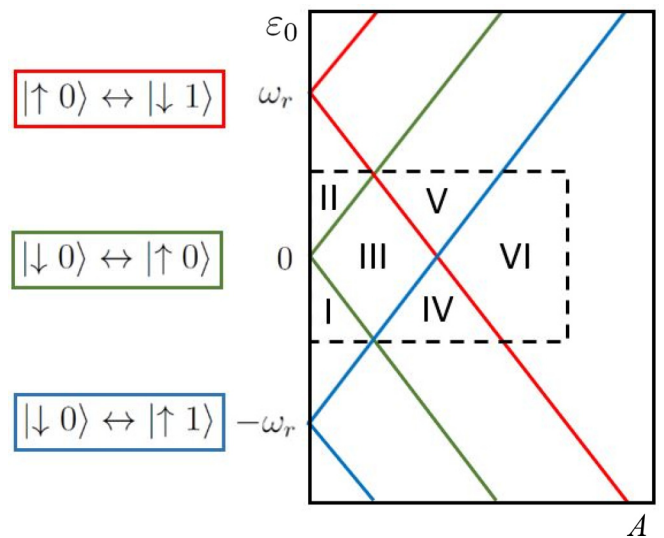


FIG. 5. (Solid lines) Scheme of the boundaries of the regions where the LZS resonances mediated by the different avoided crossings occur in plots of $\bar{P}_{|\uparrow\rangle}$, as a function of the driving parameters ϵ_0 and A . States involved in the transitions are indicated. A rectangle in dashed lines shows the range of the parameters considered along this work.

Fig. 4(b)), which as we have already mentioned, are expected for the slow driving regime [48,49]. However in our work the slow driving regime is attained due to the increase in the value of Δ_n , instead of reducing the driving frequency ω . Additionally, the lobe-shaped resonances associated to the central qubit gap Δ are distorted for large amplitudes A in comparison to the SC ($g/\omega_r = 0.0019$) case analyzed in Fig. 4(a). Notice that the maximum value of $\bar{P}_{|\uparrow\rangle}$ in Fig. 4(b) is larger than $1/2$ due to the superposition of different resonances and in contrast to Fig. 4(a), where resonances are isolated and $\bar{P}_{|\uparrow\rangle} \leq 1/2$.

The qualitative differences exhibited between Figs. 4(a) and 4(b) are thus mainly related to the increase in the size of the photonic gaps Δ_n as g/ω_r increases from the SC to the USC regime. Notice that the qubit-LZS interference patterns correspond always to the fast driving regime as we consider $\omega = 10\Delta$ along this work.

IV. DISSIPATIVE EFFECTS

Experimentally, the system is affected by the electromagnetic environment that introduces decoherence and relaxation, affecting the quantum phase of the superposition states, and/or causing spontaneous decay of the population. Several phenomenological approaches have taken into account noise and dissipation in LZS interferometry, adding an extra broadening to the Lorentzian-shaped m -order resonances described in Eq.(4) in terms of decoherence and relaxation rates[17,19]. However these approximations fail to describe the structure of the LZS patterns in the presence of dissipation in the case of strongly driven qubits [30,31], since they are valid either for large frequencies, or for low ac amplitudes, or for timescales smaller than the relaxation time. Here we study dissipative effects in LZS interferometry beyond these phenomenological approaches, using the Floquet-Born-Markov formalism for time-periodic Hamiltonians, which allows for an exact

treatment of driving protocols of arbitrary strength and frequency [31,33,34].

To study the quantum dynamics of the system coupled to the environment, we consider that the resonator is weakly coupled to a thermal reservoir modeled as an infinite set of noninteracting harmonic oscillators [55]. This assumption is justified in typical cQED architectures in which the superconducting qubit is fabricated inside a transmission line resonator [1,42]. Thus, when the qubit and the resonator are off-resonant ($\omega_q \neq \omega_r$), the resonator effectively acts as a filter of the environmental noise for the qubit. As a result, the qubit coherence times are enhanced because it is only indirectly coupled to the external noise sources through the transmission line. It should be noted that in some flux qubits [9,39], quasiparticle and dielectric losses in the qubits were identified as likely sources of energy damping. However, for simplicity, in what follows, we will neglect decay mechanisms in the qubit (i.e., qubit-reservoir terms will not be considered in the model Hamiltonian). This is appropriate for qubits that are ‘‘Purcell limited’’ [1,9,56].

The general theoretical approach to study open systems is to consider a total (system plus bath) Hamiltonian given by

$$H(t) = H_S(t) + H_B + H_{SB}, \quad (6)$$

where H_S is the system Hamiltonian and

$$H_B = \sum_{\nu} \omega_{\nu} b_{\nu}^{\dagger} b_{\nu},$$

$$H_{SB} = (a + a^{\dagger}) \sum_{\nu} c_{\nu} (b_{\nu} + b_{\nu}^{\dagger}) + (a + a^{\dagger})^2 \sum_{\nu} \frac{c_{\nu}^2}{\omega_{\nu}}, \quad (7)$$

are the terms for the bath and the system-bath interaction. In the cQED architecture considered here, the bath oscillators have frequencies ω_{ν} , with b_{ν}^{\dagger} (b_{ν}) the creation (annihilation) operators, and are linearly coupled to the resonator operator ($a + a^{\dagger}$), with coupling strength c_{ν} . Following the usual approach, the bath is characterized by a continuous distribution of modes with an Ohmic spectral density $J(\omega) = \kappa \omega e^{-\omega/\omega_D}$, with damping constant κ and cutoff frequency ω_D .

The time evolution of the reduced density matrix is computed after expanding $\rho(t)$ in terms of the time-periodic Floquet basis, $\rho_{\alpha\beta}(t) = \langle \alpha(t) | \rho(t) | \beta(t) \rangle$, and performing the Born (weak coupling) and Markov (fast relaxation) approximations. The resulting Floquet-Born-Markov (FBM) master equation [34] is solved numerically, and with it we compute $\bar{P}_{|\uparrow\rangle}(t)$. For details on these calculations we refer the reader to Refs. [31,32,57].

We consider the system as composed by the qubit and the resonator and described by the DR Hamiltonian (2). Following the Born approximation, the resonator is assumed as weakly coupled to the Ohmic thermal reservoir. Thus, for the numerical results—and consistent with typical experimental parameters—we take $\kappa = 0.001$, corresponding to weak dissipation, and a large cutoff frequency $\omega_D = 12.5\omega_r$. The bath temperature is $T = 0.0175 \omega_r/k_B$ (~ 20 mK). In Fig. 6, we plot $\bar{P}_{|\uparrow\rangle}(t)$ (for the initial condition $|\downarrow, 0\rangle$) as a function of A and ε_0 in the strong coupling case, for $g/\omega_r = 0.0019$.

First, we describe in Fig. 6(a) the results for finite time $t = 1000\tau$. At this finite time, the spectroscopic pattern still reflects the effect of the initial condition $|\downarrow, 0\rangle$, and resembles

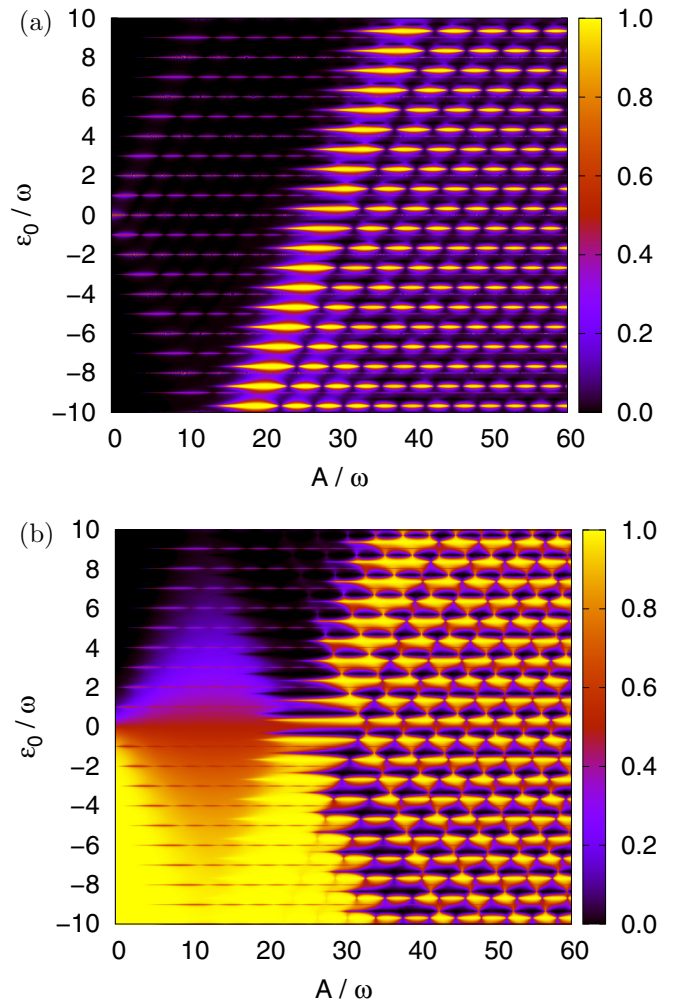


FIG. 6. LZS interference patterns for the Rabi Hamiltonian in the SC Regime ($g/\omega_r = 0.0019$) considering effects of dissipation. Plots of $\bar{P}_{|\uparrow\rangle}(t)$ as a function of the driving parameters A and ε_0 , at finite time $t = 1000\tau$ (a) and in the asymptotic regime $t = \infty$ (b). The calculations were performed for $\omega/\omega_r = 0.0375$, $\Delta/\omega_r = 0.0038$, $T = 0.0175 \omega_r/k_B$, and $\kappa = 0.001$ (see text for details).

the one obtained for the unitary evolution, Fig. 4(a). However, when we compare both patterns two main differences emerge in Fig. 6(a): (i) the resonances associated to the photonic gaps at $\varepsilon = -\omega_r$ are broadened and (ii) the probability $\bar{P}_{|\uparrow\rangle}(t)$ takes values close to 1. These features are better seen in Fig. 7(a), where we plot $\bar{P}_{|\uparrow\rangle}$ as a function of ε_0 for $A/\omega = 35$. In the case of the unitary evolution, we observe narrow peaks corresponding to the qubit resonances at $\varepsilon_0 = n\omega$ and peaks corresponding to the photonic resonances at $\varepsilon_0 = -\omega_r + m\omega$. After adding dissipation, the qubit resonances stay narrow due to the Purcell effect [1,56], which strongly reduces the qubit relaxation rate by a factor $g^2/\delta_0^2 \sim 10^{-6}$. On the other hand, the photonic resonances broaden since they are directly affected by the cavity-bath relaxation. Moreover, at the photonic resonance the probability takes values close to $\bar{P}_{|\uparrow\rangle} = 1$. There is a transfer of population among the $|\downarrow, 0\rangle \leftrightarrow |\uparrow, 1\rangle$ states followed by decay transitions $|\uparrow, 1\rangle \rightarrow |\uparrow, 0\rangle$ induced by the dissipative coupling with the bath. In this way, when the initial condition is $|\downarrow, 0\rangle$ the effect of the ac drive and

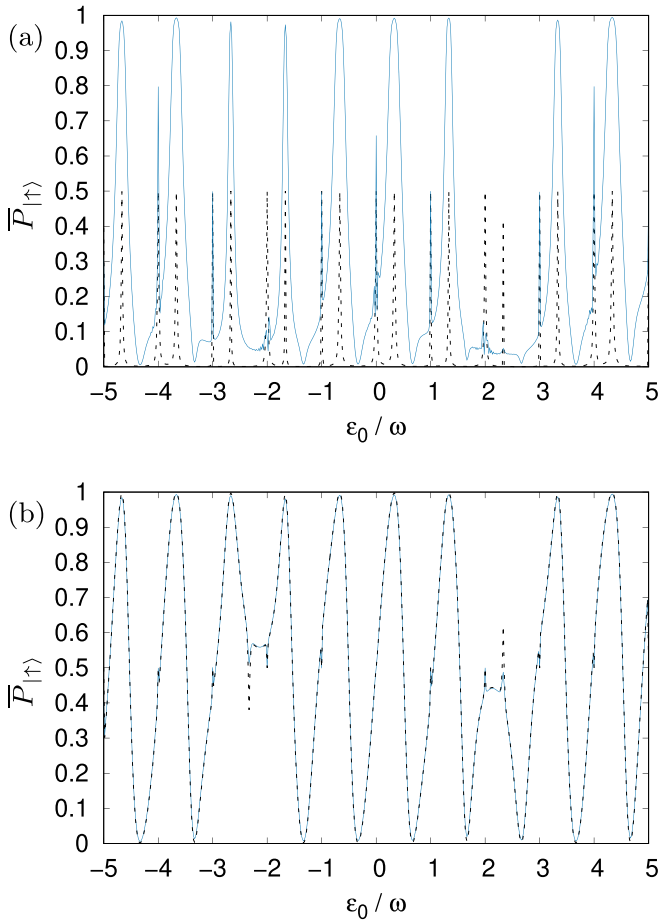


FIG. 7. (a) Averaged transition probability for the closed system $\bar{P}_{|\uparrow\rangle}$ (dashed line) and considering effects of dissipation at finite time $\bar{P}_{|\uparrow\rangle}(t \rightarrow 1000\tau)$ (solid line) as a function of ε_0 for $g/\omega_r = 0.0019$ and $A = 35\omega$. (b) Averaged transition probability in the asymptotic regime $\bar{P}_{|\uparrow\rangle}(t \rightarrow \infty)$ as a function of ε_0 for $g/\omega_r = 0.0019$ and $A = 35\omega$. Numerical results when the system is taken as qubit plus resonator (DR Hamiltonian) coupled to an Ohmic bath (solid line) and when we regard the driven qubit coupled to a structured bath (dashed lines).

the dissipation is to continuously pump population from $|\downarrow, 0\rangle$ to $|\uparrow, 0\rangle$, leading to $\bar{P}_{|\uparrow\rangle} \approx 1$. For $\varepsilon_0 > 0$, the ground state has a principal weight on state $|\downarrow, 0\rangle$, and therefore $\bar{P}_{|\uparrow\rangle} \approx 1$ corresponds to population inversion, and the resonance can be interpreted as a blue sideband resonance [31,57]. On the other hand, for $\varepsilon_0 < 0$, the ground state has a principal weight on state $|\uparrow, 0\rangle$, and therefore $\bar{P}_{|\uparrow\rangle} \approx 1$ corresponds to full cooling into the ground state, as in a red sideband resonance [31,57].

Effects of the bath are much more noticeable in the steady state regime for $t \rightarrow \infty$ [Fig. 6(b)] where the characteristic diamondlike spectroscopy patterns are easily identified. The steady state is independent of the initial condition, and thus the asymptotic pattern combines the effect of the photonic gaps at $\varepsilon_0 = -\omega_r$ and at $\varepsilon_0 = \omega_r$. This can be understood in terms of the energy spectrum shown in Fig. 1 and the different regions defined in Fig. 5.

In region I (II) of Fig. 5 where resonances are absent, only the dissipative contribution is present, and thus $\bar{P}_{|\uparrow\rangle}(t \rightarrow$

$\infty) \sim 1(0)$, respectively. Region III, corresponding to the first diamond, presents a qubit-LZS pattern with narrow lobe-shaped qubit resonances at $\varepsilon_0 = n\omega$ and a background structure due to the relaxation processes. Regions IV and V correspond to the intermediate sector between diamonds, for $\varepsilon_0 < 0$ and $\varepsilon_0 > 0$, respectively. In the second diamond sector (region VI), the combined effect of the resonances associated to the qubit gap and the two photonic gaps contribute to the LZS transitions. The photonic resonances at $\varepsilon_0 = -\omega_r + m\omega$ give maxima with $\bar{P}_{|\uparrow\rangle} \approx 1$, due to the LZS transition plus decay mechanism described above. On the other hand, the photonic resonances at $\varepsilon_0 = \omega_r + m\omega$ give $\bar{P}_{|\uparrow\rangle} \approx 0$. In this case, at the photonic resonance there is a transfer of population between $|\uparrow, 0\rangle \leftrightarrow |\downarrow, 1\rangle$ states plus dissipative decay transitions $|\downarrow, 1\rangle \rightarrow |\downarrow, 0\rangle$, leading to $\bar{P}_{|\uparrow\rangle} \approx 0$. In Fig. 7(b), we see clearly the two types of photonic resonances with alternating broad peaks with $\bar{P}_{|\uparrow\rangle} \approx 1$ and broad dips with $\bar{P}_{|\uparrow\rangle} \approx 0$, in a plot of the dependence of $\bar{P}_{|\uparrow\rangle}$ with ε_0 for $A = 35\omega$. It is also possible to notice the narrow peaks corresponding to the qubit resonances at $\varepsilon_0 = n\omega$.

For the analysis of Fig. 6(b), it is also worthwhile to mention that for $g \ll \omega_{q/r}$, a plausible assumption is to consider the quantum system solely as the qubit. In this approach, the transmission line resonator is taken as a part of the environment seen by the qubit and it is possible to map the composite (resonator-bath) reservoir to a “structured bath” of noninteracting harmonic oscillators with an effective spectral density

$$J_{\text{eff}}(\omega) = \frac{16\kappa g^2 \omega_r^2 \omega}{(\omega_r^2 - \omega^2)^2 + (\kappa\omega_r\omega)^2}, \quad (8)$$

that behaves as Ohmic at low frequencies and presents a Lorentzian peak at $\omega = \omega_r$ [31,58,59]. The qubit-structured bath coupling Hamiltonian is of the form $H_{qB} \propto \sigma_y X$, with X a coordinate of the structured bath. In Fig. 7(b), we see a good agreement between the $\bar{P}_{|\uparrow\rangle}$ obtained from the qubit coupled through σ_y to an structured bath and the corresponding results of Fig. 6(b) for the DR Hamiltonian. Within the “qubit + structured bath” scenario one can interpret the qubit LZS pattern of region III as the LZS pattern of a qubit transversely coupled to a bath, studied in Ref. [32], which is characterized by narrow resonance peaks and a background off-resonance population.

One can also compare with the LZS pattern of Ref. [31], where a qubit coupled to a structured bath through σ_z was analyzed. We can identify differences and similarities with the present work. (i) The first diamond LZS pattern of Ref. [31] presents antisymmetric resonances (characteristic of longitudinal coupling to the bath) instead of the narrow resonances and background observed here in region III of Fig. 5 (identified with the first diamond). (ii) The second diamond of the LZS pattern of Ref. [31] presents the same structure of alternating bright and dark lobes obtained here in region VI, which has been explained in terms of red and blue sidebands.

The case of ultra strong coupling ($g = 0.1125\omega_r$, shown in Fig. 8) cannot be reduced to the “qubit + structured bath” picture. In this situation, the photonic gaps $\Delta_n = 2g\sqrt{n+1}$ are larger than the driving frequency ω , and the associated

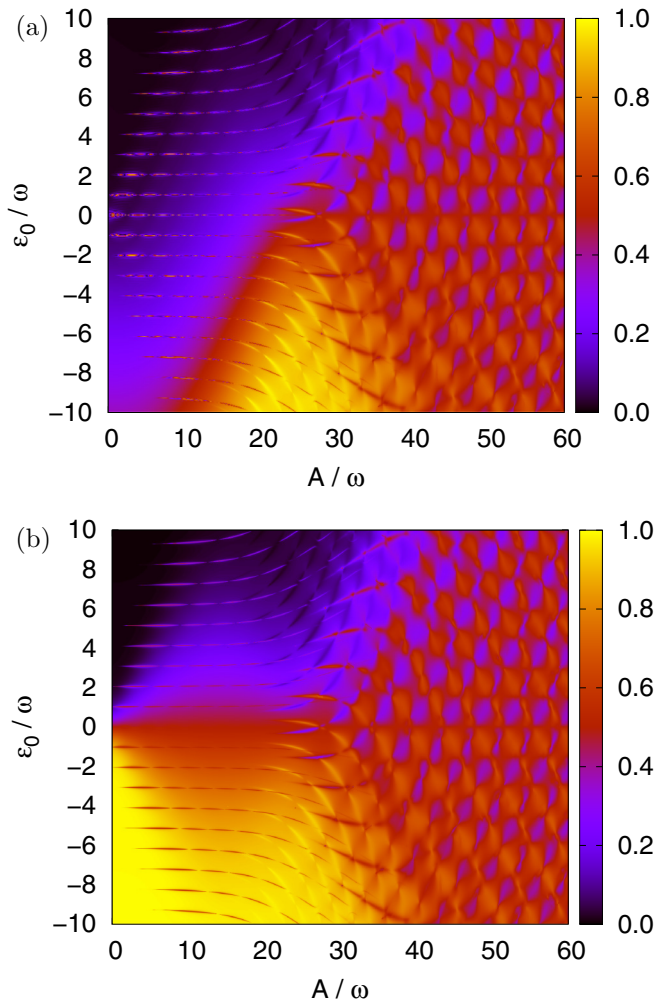


FIG. 8. LZS interference patterns for the Rabi Hamiltonian in the USC regime ($g/\omega_r = 0.1125$) considering effects of dissipation. Plots of $\bar{P}_{|\uparrow\rangle}(t)$ as a function of the driving parameters A and ε_0 , at finite time $t = 50\tau$ (a) and in the asymptotic regime $t = \infty$ (b). The calculations were performed for $\omega/\omega_r = 0.0375$, $\Delta/\omega_r = 0.0038$, $T = 0.0175 \omega_r/k_B$, and $\kappa = 0.001$ (see text for details).

photonic-LZS patterns are in the slow driving regime, as discussed in the previous section. In Fig. 8(a), we plot the LZS pattern at a finite time $t = 50\tau$. At short times, it is possible to observe the effect of the initial condition (the state $|\downarrow, 0\rangle$), and the plot resembles the results obtained for the unitary evolution in Fig. 4(b). The steady state regime is shown in Fig. 8(b). The first diamond, in region III, is similar to the one in Fig. 6(b), since it corresponds to the qubit-LZS pattern. The different behavior of the USC regime

is manifested for amplitudes A beyond the first diamond. In region IV, one can distinguish the arc-shaped photonic resonances with the arcs centered around the point $A = 0$, $\varepsilon_0 = -\omega_r$. Similarly, in region V, one can observe the arcs centered around the point $A = 0$, $\varepsilon_0 = \omega_r$, corresponding to the other photonic resonances. More interestingly, in the second diamond, region VI, the combined pattern of the intercrossing of two arc-shaped photonic resonances is observed. This later intercrossed pattern structure is an interested and novel signature of the driven cQED in the USC regime. As a final comment we stress that for the USC regime, the steady state is attained for timescales shorter than in the SC regime. In our case for $t = 1000\tau$, the LZS patterns in the USC (not shown) resemble those of the stationary case obtained in Fig. 8(b).

V. CONCLUDING REMARKS

To summarize, we have thoroughly analyzed the LZS interference patterns that arise in a realistic cQED architecture taking into account the noise effects introduced by the environment, i.e. decoherence and relaxation. We studied the system composed by a harmonically driven superconducting qubit that is transversally coupled to a transmission line resonator.

We considered different values of the qubit-resonator coupling strength corresponding to the strong coupling (SC) and ultrastrong coupling (USC) regimes and observed important differences in the resonance patterns between both situations. A comprehensive description of the results was given in terms of the energy spectrum of the system Hamiltonian. We analyzed how the environment affects the LZS patterns for different timescales and compared these results with those obtained when noise is neglected.

We identify in the LZS patterns the contributions due to the qubit gap at $\varepsilon_0 = 0$ and those due to the photonic gaps at $\varepsilon_0 = \pm\omega_r$. In particular, it was shown that for large amplitudes the interference patterns can be interpreted as the combined intercrossing of patterns of qubit-LZS and photonic-LZS.

Dissipative effects induce dramatic changes in the structure of the LZS patterns in comparison to the ideal (noiseless) case. The features analyzed along this work could help to design better strategies to mitigate noise in LZS interferometry, opening the possibility to extend the field of cQED for the case of strongly driven qubits.

ACKNOWLEDGMENTS

We acknowledge financial support from CNEA, CONICET (PIP11220150100756), UNCuyo (P 06/C455) and ANPCyT (PICT2014-1382, PICT2016-0791).

- [1] A. Blais, R.-S. Huang, A. Wallraff, S. M. Girvin, and R. J. Schoelkopf, *Phys. Rev. A* **69**, 062320 (2004).
 [2] A. Wallraff, D. I. Schuster, A. Blais, L. Frunzio, R.-S. Huang, J. Majer, S. Kumar, S. M. Girvin, and R. J. Schoelkopf, *Nature (London)* **431**, 162 (2004).

- [3] Z.-L. Xiang, S. Ashhab, J. Q. You, and F. Nori, *Rev. Mod. Phys.* **85**, 623 (2013).
 [4] A. Blais, S. M. Girvin, and W. Oliver, *Nat. Phys.* **16**, 247 (2020).
 [5] X. Gu, A. F. Kockum, A. Miranowicz, Y.-X. Liu, and F. Nori, *Phys. Rep.* **718-719**, 1 (2017).

- [6] A. Dewes, R. Lauro, F. R. Ong, V. Schmitt, P. Milman, P. Bertet, D. Vion, and D. Esteve, *Phys. Rev. B* **85**, 140503(R) (2012).
- [7] L. DiCarlo, J. M. Chow, J. M. Gambetta, L. S. Bishop, B. R. Johnson, D. I. Schuster, J. Majer, A. Blais, L. Frunzio, S. M. Girvin, and R. J. Schoelkopf, *Nature (London)* **460**, 240 (2009).
- [8] L. DiCarlo, M. D. Reed, L. Sun, B. R. Johnson, J. M. Chow, J. M. Gambetta, L. Frunzio, S. M. Girvin, M. H. Devoret, and R. J. Schoelkopf, *Nature (London)* **467**, 574 (2010).
- [9] M. Stern, G. Catelani, Y. Kubo, C. Grezes, A. Bienfait, D. Vion, D. Esteve, and P. Bertet, *Phys. Rev. Lett.* **113**, 123601 (2014).
- [10] P. Campagne-Ibarcq, E. Zalys-Geller, A. Narla, S. Shankar, P. Reinhold, L. Burkhardt, C. Axline, W. Pfaff, L. Frunzio, R. J. Schoelkopf, and M. H. Devoret, *Phys. Rev. Lett.* **120**, 200501 (2018).
- [11] H. Paik, D. I. Schuster, L. S. Bishop, G. Kirchmair, G. Catelani, A. P. Sears, B. R. Johnson, M. J. Reagor, L. Frunzio, L. I. Glazman, S. M. Girvin, M. H. Devoret, and R. J. Schoelkopf, *Phys. Rev. Lett.* **107**, 240501 (2011).
- [12] B. R. Johnson, M. D. Reed, A. A. Houck, D. I. Schuster, L. S. Bishop, E. Ginossar, J. M. Gambetta, L. DiCarlo, L. Frunzio, S. M. Girvin, and R. J. Schoelkopf, *Nat. Phys.* **6**, 663 (2010).
- [13] T. Walter, P. Kurpiers, S. Gasparinetti, P. Magnard, A. Potočnik, Y. Salathé, M. Pechal, M. Mondal, M. Oppliger, C. Eichler, and A. Wallraff, *Phys. Rev. Appl.* **7**, 054020 (2017).
- [14] A. F. van Loo, A. Fedorov, K. Lalumiere, B. C. Sanders, A. Blais, and A. Wallraff, *Science* **342**, 1494 (2013).
- [15] C. Eichler, C. Lang, J. M. Fink, J. Govenius, S. Filipp, and A. Wallraff, *Phys. Rev. Lett.* **109**, 240501 (2012).
- [16] N. Didier, J. Bourassa, and A. Blais, *Phys. Rev. Lett.* **115**, 203601 (2015).
- [17] S. Shevchenko, S. Ashhab, and F. Nori, *Phys. Rep.* **492**, 1 (2010).
- [18] W. D. Oliver, Y. Yu, J. C. Lee, K. K. Berggren, L. S. Levitov, and T. P. Orlando, *Science* **310**, 1653 (2005).
- [19] D. M. Berns, W. D. Oliver, S. O. Valenzuela, A. V. Shytov, K. K. Berggren, L. S. Levitov, and T. P. Orlando, *Phys. Rev. Lett.* **97**, 150502 (2006).
- [20] D. M. Berns, M. S. Rudner, S. O. Valenzuela, K. K. Berggren, W. D. Oliver, L. S. Levitov, and T. P. Orlando, *Nature (London)* **455**, 51 (2008).
- [21] W. D. Oliver and S. O. Valenzuela, *Quantum Inf. Process* **8**, 261 (2009).
- [22] A. Izmalkov, S. H. W. van der Ploeg, S. N. Shevchenko, M. Grajcar, E. Il'ichev, U. Hübner, A. N. Omelyanchouk, and H.-G. Meyer, *Phys. Rev. Lett.* **101**, 017003 (2008).
- [23] M. Sillanpää, T. Lehtinen, A. Paila, Y. Makhlin, and P. Hakonen, *Phys. Rev. Lett.* **96**, 187002 (2006).
- [24] C. M. Wilson, T. Duty, F. Persson, M. Sandberg, G. Johansson, and P. Delsing, *Phys. Rev. Lett.* **98**, 257003 (2007).
- [25] J. R. Petta, H. Lu, and A. C. Gossard, *Science* **327**, 669 (2010).
- [26] H. Ribeiro, J. R. Petta, and G. Burkard, *Phys. Rev. B* **87**, 235318 (2013).
- [27] F. Forster, G. Petersen, S. Manus, P. Hänggi, D. Schuh, W. Wegscheider, S. Kohler, and S. Ludwig, *Phys. Rev. Lett.* **112**, 116803 (2014).
- [28] R. Blattmann, P. Hänggi, and S. Kohler, *Phys. Rev. A* **91**, 042109 (2015).
- [29] X. Mi, S. Kohler, and J. R. Petta, *Phys. Rev. B* **98**, 161404(R) (2018).
- [30] A. Ferrón, D. Domínguez, and M. J. Sánchez, *Phys. Rev. Lett.* **109**, 237005 (2012).
- [31] A. Ferrón, D. Domínguez, and M. J. Sánchez, *Phys. Rev. B* **93**, 064521 (2016).
- [32] A. L. Gramajo, D. Domínguez, and M. J. Sánchez, *Phys. Rev. B* **100**, 075410 (2019).
- [33] M. Grifoni and P. Hänggi, *Phys. Rep.* **304**, 229 (1998).
- [34] S. Kohler, R. Utermann, P. Hänggi, and T. Dittrich, *Phys. Rev. E* **58**, 7219 (1998).
- [35] D. Zueco, P. Hänggi, and S. Kohler, *New J. Phys.* **10**, 115012 (2008).
- [36] M. P. Silveri, K. S. Kumar, J. Tuorila, J. Li, A. Vepsäläinen, E. V. Thuneberg, and G. S. Paroanu, *New J. Phys.* **17**, 043058 (2015).
- [37] S. Gustavsson, J. Bylander, F. Yan, P. Forn-Díaz, V. Bolkhovskiy, D. Braje, G. Fitch, K. Harrabi, D. Lennon, J. Miloshi, P. Murphy, R. Slattey, S. Spector, B. Turek, T. Weir, P. B. Welander, F. Yoshihara, D. G. Cory, Y. Nakamura, T. P. Orlando, and W. D. Oliver, *Phys. Rev. Lett.* **108**, 170503 (2012).
- [38] M. Kervinen, J. E. Ramírez-Muñoz, A. Välimaa, and M. A. Sillanpää, *Phys. Rev. Lett.* **123**, 240401 (2019).
- [39] F. Yan, S. Gustavsson, A. Kamal, J. Birenbaum, A. P. Sears, D. Hover, T. J. Gudmundsen, D. Rosenberg, G. Samach, S. Weber, J. L. Yoder, T. P. Orlando, J. Clarke, A. J. Kerman, and W. D. Oliver, *Nat. Commun.* **7**, 12964 (2016).
- [40] I. Chiorescu, P. Bertet, K. Semba, Y. Nakamura, C. J. P. M. Harmans, and J. E. Mooij, *Nature* **431**, 159 (2004).
- [41] T. Niemczyk, F. Deppe, H. Huebl, E. P. Menzel, F. Hocke, M. J. Schwarz, J. J. Garcia-Ripoll, D. Zueco, T. Hümmer, E. Solano, A. Marx, and R. Gross, *Nat. Phys.* **6**, 772 (2010).
- [42] F. Yan, D. Campbell, P. Krantz, M. Kjaergaard, D. Kim, J. L. Yoder, D. Hover, A. Sears, A. J. Kerman, T. P. Orlando, S. Gustavsson, and W. D. Oliver, *Phys. Rev. Lett.* **120**, 260504 (2018).
- [43] P. Forn-Díaz, L. Lamata, E. Rico, J. Kono, and E. Solano, *Rev. Mod. Phys.* **91**, 025005 (2019).
- [44] J. H. Shirley, *Phys. Rev.* **138**, B979 (1965).
- [45] S.-K. Son, S. Han, and S.-I. Chu, *Phys. Rev. A* **79**, 032301 (2009).
- [46] A. Ferrón and D. Domínguez, *Phys. Rev. B* **81**, 104505 (2010).
- [47] J. Stehlik, Y. Dovzhenko, J. R. Petta, J. R. Johansson, F. Nori, H. Lu, and A. C. Gossard, *Phys. Rev. B* **86**, 121303(R) (2012).
- [48] J. V. Koski, A. J. Landig, A. Pályi, P. Scarlino, C. Reichl, W. Wegscheider, G. Burkard, A. Wallraff, K. Ensslin, and T. Ihn, *Phys. Rev. Lett.* **121**, 043603 (2018).
- [49] S. N. Shevchenko, A. I. Ryzhov, and F. Nori, *Phys. Rev. B* **98**, 195434 (2018).
- [50] A. L. Gramajo, D. Campbell, B. Kannan, D. K. Kim, A. Melville, B. M. Niedzielski, J. L. Yoder, M. J. Sánchez, D. Domínguez, S. Gustavsson, and W. D. Oliver, *Phys. Rev. Applied* (to be published), [arXiv:1912.12488](https://arxiv.org/abs/1912.12488).
- [51] S. Agarwal, S. M. H. Rafsanjani, and J. H. Eberly, *J. Phys. B: At. Mol. Opt. Phys.* **46**, 224017 (2013).
- [52] Q. Xie, H. Zhong, M. T. Batchelor, and C. Lee, *J. Phys. A: Math. Theor.* **50**, 113001 (2017).
- [53] A. Ferrón, D. Domínguez, and M. J. Sánchez, *Phys. Rev. B* **82**, 134522 (2010).
- [54] S. Ashhab, J. R. Johansson, A. M. Zagoskin, and F. Nori, *Phys. Rev. A* **75**, 063414 (2007).

- [55] H.-P. Breuer and F. Petruccione, *The Theory of Open Quantum Systems* (Oxford University Press, Oxford, England, 2006).
- [56] E. A. Sete, J. M. Gambetta, and A. N. Korotkov, *Phys. Rev. B* **89**, 104516 (2014).
- [57] J. Hausinger and M. Grifoni, *Phys. Rev. A* **81**, 022117 (2010).
- [58] A. Garg, *J. Chem. Phys.* **83**, 4491 (1985).
- [59] M. C. Goorden, M. Thorwart, and M. Grifoni, *Phys. Rev. Lett.* **93**, 267005 (2004).